

Access to Metal Centers and Fluxional Hydride Coordination Integral for CO₂ Insertion into [Fe₃(μ-H)₃]³⁺ Clusters

Dae Ho Hong, Ricardo B. Ferreira, Vincent J. Catalano, Ricardo García-Serres, Jason Shearer,* and Leslie J. Murray*

Cite This: <https://doi.org/10.1021/acs.inorgchem.1c00244>

Read Online

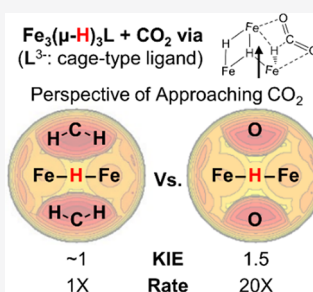
ACCESS |

Metrics & More

Article Recommendations

Supporting Information

ABSTRACT: CO₂ insertion into tri(μ-hydrido)triiron(II) clusters ligated by a tris(β-diketiminate) cyclophane is demonstrated to be balanced by sterics for CO₂ approach and hydride accessibility. Time-resolved NMR and UV–vis spectra for this reaction for a complex in which methoxy groups border the pocket of the hydride donor (Fe₃H₃L², **4**) result in a decreased activation barrier and increased kinetic isotope effect consistent with the reduced sterics. For the ethyl congener Fe₃H₃L¹ (**2**), no correlation is found between rate and reaction solvent or added Lewis acids, implying CO₂ coordination to an Fe center in the mechanism. The estimated hydricity (50 kcal/mol) based on observed H/D exchange with BD₃ requires Fe–O bond formation in the product to offset an endergonic CO₂ insertion. μ₃-hydride coordination is noted to lower the activation barrier for the first CO₂ insertion event in DFT calculations.

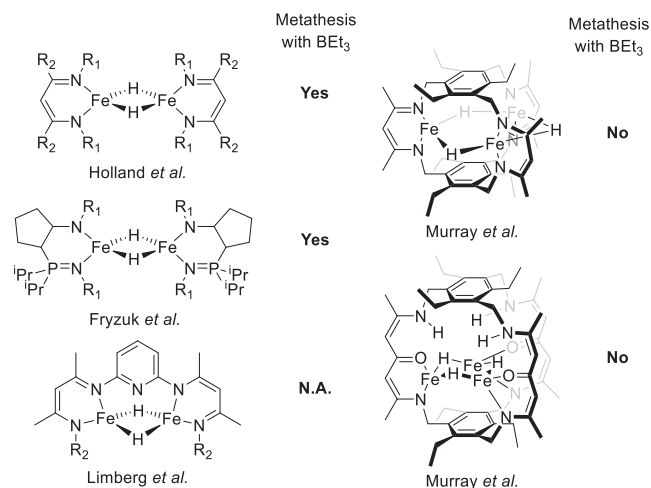


INTRODUCTION

Metal hydrides mediate various small molecule transformations in chemical and biological systems, including proton, CO₂, and N₂ reduction.^{1–7} Given such reactivity, metal hydrides have gathered substantial interest, especially in the context of renewable energy and carbon-neutral fuel synthesis as well as fertilizer production.^{8–12} Mononuclear metal hydrides have been extensively studied in the fields of energy storage,¹³ electrocatalysis,^{14,15} and chemical synthesis.^{16,17} Metal hydride compounds have predominantly employed strong field ligands, leading to well-defined acid–base reactivity profiles observed in many compounds. Far fewer examples of metal-hydride-supported weak-field donors are known, and even fewer in which the hydrides adopt bridging coordination modes. Such hydride-bridged multimetallic assemblies are proposed as key intermediates in the activation of small molecules affected by metalloenzymes and heterogeneous catalysts. Notable examples of important hydride-bridged transients include the proposed structures of reduced intermediates of the FeMo cofactor from molybdenum-dependent nitrogenases and of [NiFe]- or [FeFe]-hydrogenases,^{7,18–20} H adatoms on the surface of various heterogeneous catalysts,^{21–23} and copper hydride clusters used to catalyze organic transformations (e.g., conjugate reduction reactions).^{24,25} Describing the factors governing reactivity of weak field supported hydride-bridged metal centers has broad relevance to chemical synthesis, industrial processes, and biological systems.

Weak-field ligands in which steric bulk limits the coordination number afford metal hydrides with diverse reactivity profiles, including reductive elimination, insertion, and H atom transfer reactivity (Scheme 1).^{26–34} For example, Holland and co-workers synthesized a series of β-diketiminate

Scheme 1. Reported Multi-Iron Complexes with Bridging Hydrides Coordinated by β-Diketiminate-Type Ligands



(or BDI) supported di(μ-hydrido)diiron complexes in which the H/D exchange with H₂/D₂ and between isotopologues, bond metathesis with BET₃, insertion reactivity with CO₂ and various other possible electrophiles, and H₂ reductive elimination have been observed.^{35,36} In contrast to these

Received: February 1, 2021

dimetallics which spontaneously assemble and exist in a monomer–dimer equilibrium, the tri(μ -hydrido)triiron complex templated by a tris(β -diketimine)cyclophane (i.e., $\text{Fe}_3(\mu\text{-H})_3\text{L}^1$ or **2**) is remarkably specific for hydride transfer to CO_2 with minimal or no hydride transfer reactivity to other substrates.²⁹ Similar hydride transfer reactivity was also observed for the cobalt and the zinc congeners, leading to a hypothesis that the ligand pocket surrounding the μ -hydride donors strongly influences kinetics and selectivity for CO_2 reduction to formate.^{29,34,37} In addition, we also observed reductive elimination (re) of H_2 upon the reaction of **2** with CO . The resultant $\text{Fe}_3(\mu_3\text{-H})(\text{CO})_2\text{L}^1$ product is competent for the oxidative addition of H_2 at slightly elevated temperatures to regenerate **2**. Such reactivity suggested that the hydrides in **2** are fluxional as the hydride–hydride distances are substantially longer than that in H_2 .³⁴ A detailed understanding of the order of Fe–H bond breaking and C–H bond formation and the factors governing the observed substrate specificity are important for developing approaches to controlling specificity and reactivity. Herein, we report the effect of changes to the secondary coordination sphere—specifically, the consequence of a methoxy for ethyl substitution—on the rate of CO_2 insertion, effect of solvent and exogenous Lewis acids on reaction of **2** with CO_2 , hydride exchange between and transfer from **2** to boranes, and density functional theory simulations of the reaction coordinate for transfer of the first hydride to CO_2 to generate the monoformate complex. The mechanistic picture that emerges is one in which hydrides shift coordination modes upon interaction with the substrate, an Fe–OCO interaction precedes hydride transfer—although this interaction is intimately related to the steric constraints—and sterics of the pocket surrounding the hydride and the hydricity enforce the observed substrate selectivity.

EXPERIMENTAL METHODS

General Considerations. All manipulations except ligand synthesis were performed inside an N_2 -filled Innovative Technologies glovebox unless otherwise stated. Tetrahydrofuran (THF), benzene, toluene, and *n*-hexane were purchased from Sigma-Aldrich, then dried using an Innovative Technologies solvent purification system, transferred under an inert atmosphere to the anaerobic chamber, and stored over activated 3 Å molecular sieves for at least 24 h prior to use. Benzene- d_6 , toluene- d_8 , and THF- d_8 were purchased from Cambridge Isotope Laboratories, dried over CaH_2 or Na/benzophenone under reflux, then distilled, degassed, and stored over 3 Å molecular sieves.

^1H nuclear magnetic resonance (^1H NMR) spectra were recorded on a 500 MHz Varian Inova spectrometer or a 300 MHz Mercury spectrometer equipped with a three-channel 5 mm indirect detection probe with z -axis gradients. Chemical shifts were reported in δ (ppm) and were referenced to solvent resonances of $\delta\text{H} = 7.16$ ppm for benzene- d_6 , 7.01 ppm for toluene- d_8 , and 3.58 ppm for THF- d_8 . Fourier transform infrared (FT-IR) spectra were recorded as solids on a Thermo Fisher iSS instrument equipped with an ATR diamond iD7 stage and operated by the OMNIC software package. H_3L^1 , $\text{Fe}_3\text{Br}_3\text{L}^1$ (**1**),³⁸ $\text{Fe}_3\text{H}_3\text{L}^1$ (**2**),²⁹ and 1,3,5-tri(bromomethyl)-2,4,6-trimethoxybenzene³⁹ were prepared following the previous literature.

1,3,5-Tri(azidomethyl)-2,4,6-trimethoxybenzene. The title compound was synthesized using the protocol described for 1,3,5-tri(azidomethyl)-2,4,6-triethylbenzene.⁴⁰ Briefly, 1,3,5-tri(bromomethyl)-2,4,6-trimethoxybenzene (6.51 g, 14.6 mmol) was dissolved in acetone (150 mL) and treated with NaN_3 (3.80 g, 58.4 mmol, 4.0 equiv), and the white suspension was heated to reflux. H_2O (40 mL) was then added dropwise, and the mixture was stirred at 50 °C for 12 h. The product was extracted with dichloromethane and the

organic phase dried under a vacuum to yield an orange-red oil (4.81 g, 14.4 mmol, yield 99%). ^1H NMR (300 MHz, CDCl_3 , 298 K): δ 4.45 (s, 6 H), 3.92 (s, 9 H).

1,3,5-Tri(aminomethyl)-2,4,6-trimethoxybenzene. The title compound was synthesized by a procedure analogous to that for 1,3,5-tri(aminomethyl)-2,4,6-triethylbenzene.⁴¹ 1,3,5-Tri(azidomethyl)-2,4,6-trimethoxybenzene (4.81 g, 14.4 mmol) and Pd/C (10 wt % Pd, 0.200 g, 0.188 mmol, 1.3 mol %) were suspended in ethanol (100 mL) and transferred to a Parr bomb. The system was charged with H_2 (700 psi) under stirring in an ice–water bath and then allowed to warm to room temperature and then was stirred for 2 days. The resulting mixture was filtered over the ethanol-rinsed Celite pad in a fine glass frit. Volatiles of the filtrate were removed under a vacuum, resulting in a pale-yellow powder (3.54 g, 13.9 mmol, yield 96%). ^1H NMR (300 MHz, CDCl_3 , 298 K): δ 3.84 (s, 6 H), 3.82 (s, 9 H).

H_3L^2 . 1,3,5-tri(aminomethyl)-2,4,6-trimethoxybenzene (3.54 g, 13.9 mmol) and 2,4-pentanedione-2,2-(ethylene glycol) monoketal (3.26 g, 22.2 mmol, 1.6 equiv) were dissolved in methanol (100 mL). The mixture was brought to reflux under dinitrogen for 2 days, when a pale-yellow suspension was formed. The mixture was then cooled to room temperature and filtered through a fine fritted glass funnel. The resulting pale-yellow powder was washed with methanol (3 \times 30 mL) and water (3 \times 30 mL) and dried under a vacuum. Yield: 3.18 g (65%). ^1H NMR (300 MHz, CDCl_3 , 298 K): δ 10.48 (br s, 3 H), 4.56 (s, 3 H), 4.31 (s, 12 H), 3.64 (s, 18 H), 2.03 (s, 18 H). $^{13}\text{C}\{^1\text{H}\}$ NMR (126 MHz, CDCl_3 , 298 K): δ : 160.03, 158.87, 123.34, 110.14, 93.79, 63.82, 40.85, 20.23. (+)ESI-MS ($[\text{M} + \text{H}]^+$) m/z calcd. for $\text{C}_{39}\text{H}_{54}\text{N}_6\text{O}_6$: 703.4183. Found: 703.4197.

$\text{Fe}_3\text{Br}_3\text{L}^2$ (3**).** H_3L^2 (217 mg, 0.308 mmol) and lithium LiN^iPr_2 (LDA, 134 mg, 1.22 mmol, 4.0 equiv) were combined with THF (4 mL) and stirred for 10 min to afford a purple solution. All volatiles were removed from the solution, and the resulting dark purple residue was combined with FeBr_2 (315 mg, 1.46 mmol, 4.7 equiv) and toluene (20 mL). The mixture was stirred at 50 °C for 20 h, then the dark red mixture was filtered over the toluene-rinsed Celite pad, and the filtrate was cooled down to -34 °C for 2 days, where dark red crystals were obtained (149 mg, 0.127 mmol, yield 42%). Crystals suitable for X-ray diffraction were grown by slow evaporation of a saturated toluene solution of the complex. ^1H NMR (500 MHz, benzene- d_6 , 298 K): δ : 250.06 (2 H), 208.67 (2 H), 128.91 (4 H), 41.20 (4 H), 17.99 (6 H), 3.62 (1 H), -5.26 (12 H), -32.55 (18 H), -82.29 (2 H). FT-IR ν (cm^{-1}): 2920, 1579, 1512, 1390, 1338, 1100, 1004, 736, 572. Mößbauer parameters (80 K, zero-applied field, mm/s): $\delta/\Delta E_{\text{Q}} = 0.90/2.47$ and $0.93/1.72$. Combustion Anal. exp.(calc.) for $\text{C}_{44.25}\text{H}_{57}\text{Br}_3\text{Fe}_3\text{N}_6\text{O}_6$ ($\text{Fe}_3\text{Br}_3\text{L}^2\cdot 0.75\text{C}_7\text{H}_8$): C, 45.27(45.19); H, 4.80(4.88); N, 7.02(7.15).

$\text{Fe}_3\text{H}_3\text{L}^2$ (4**).** **3** (134 mg, 0.121 mmol) was combined with toluene (4 mL), resulting in a red suspension at room temperature. To this suspension, a solution of KBET_3H (49.2 mg, 0.357 mmol, 3.0 equiv) in toluene (2 mL) was added dropwise under vigorous stirring. The system turned red-brown upon addition, and it was kept under 25 °C for 10 min. The resulting dark red-orange mixture was filtered over a Nylon filter paper, resulting in a black residue that was washed with toluene (2 mL). The combined filtrate was evaporated under reduced pressure to afford a dark brown solid. This dark brown solid was recrystallized in cold diethyl ether at -35 °C (72.5 mg, 0.077 mmol, yield 64%). ^1H NMR (500 MHz, benzene- d_6 , 298 K): δ (ppm): 73.70 (12 H), 2.28 (3 H), -16.81 (18 H), -29.15 (18 H). FT-IR ν (cm^{-1}): 2918, 1592, 1522, 1397, 1348, 1343, 1228, 1112, 1008, 741, 499. Mößbauer parameters (80 K, zero-applied field, mm/s): $\delta/\Delta E_{\text{Q}} = 0.78/2.27$. Combustion anal. exp. (calc.) for $\text{C}_{45}\text{H}_{69}\text{Fe}_3\text{N}_6\text{O}_{7.5}$ ($\text{Fe}_3\text{H}_3\text{L}^2\cdot 1.5\text{Et}_2\text{O}$): C, 55.18(55.06); H, 6.58(7.09); N, 8.62(8.56).

$\text{Fe}_3(\text{CO}_2\text{H})_3\text{L}^2$ (6c**).** A solution of **4** in a benzene- d_6 was reacted with CO_2 as described in NMR kinetic experiment below except the temperature was maintained at 50 °C. After 2 days, the resulting product was subjected to analysis. ^1H NMR (500 MHz, benzene- d_6 , 298 K) δ (ppm): 216.64, 100.38, -2.66 , -4.92 , -7.08 , -33.01 , -49.84 . FT-IR ν (cm^{-1}): 2916, 1938, 1690 (C=O of formate), 1520,

1401, 1340, 1105, 1005, 798. (+)ESI-MS ($[M+2H]^+$) m/z calcd. for $C_{42}H_{56}Fe_3N_6O_{12}$: 1004.2005. Found: 1004.2347.

X-ray Crystallography. Single crystal X-ray diffraction was performed on a Bruker SMART Apex II CCD instrument at 100 K using graphite-monochromated Mo $K\alpha$ radiation. The crystals were covered in Paratone oil and mounted on glass fibers. Lorentz and polarization effects were corrected using SAINT, and the absorption corrections were applied using SADABS. The structures were solved using direct methods or Patterson syntheses using SHELXS and SHELXL.

Möbbauser Spectroscopy. In a N_2 -filled glovebox, samples were ground into fine powders, placed in Delrin sample containers, and sealed. Möbbauser spectra were measured either on a low-field Möbbauser spectrometer equipped with a closed-cycle SHI-850-5 cryostat from Janis and SHI or an Oxford Instruments Spectromag 4000 cryostat containing an 8 T split-pair superconducting magnet. Both spectrometers were operated in constant acceleration mode in transmission geometry. The isomer shifts are referenced against a room temperature metallic iron foil. Analysis of the data was performed using the program WMOSS (WEB Research).

NMR Kinetic Experiments: Reaction of 4 with CO_2 . A solution of 4 in a benzene- d_6 and a capillary charged with a hexamethylbenzene standard solution were transferred to a J-Young NMR tube, and the tube was degassed by five cycles of freeze–pump–thaw. Concurrently, a 50 mL Schlenk flask was evacuated and charged with CO_2 , and CO_2 was transferred from this flask to the headspace of an NMR tube using a three-way valve. The NMR tube valve was then closed, and the tube was quickly shaken several times. The equilibrated CO_2 concentration was determined by the following equation:

$$[CO_2]_{eqm} = n_{CO_2, total} \gamma_{soln} / V_{soln}$$

$$\gamma_{soln} = 1 / (1 + \mathcal{H}(V_{head} + V_{flask}) / n_{soln} RT)$$

where R , γ_{soln} , V_{soln} , V_{head} , V_{flask} and n_{soln} are the ideal gas constant, the ratio of CO_2 remained in solution, the volume of the solution, the headspace volume of the J-young NMR tube, the volume of the Schlenk flask, and moles of solvent, respectively. The Henry constants, \mathcal{H} , of benzene and toluene are 10.370×10^6 and 9.705×10^6 Pa, respectively, at 298.15 K.⁴²

NMR spectra were measured up to 7 days, with each spectrum measured using the same power, gain, and shimming parameters. After phase correction and reference peak assignment, baseline correction was performed using a Whittaker smoother method (filter: 50, 28.57 Hz; smooth factor: 10^6) provided by MestReNova 8.1. Common integration ranges were used for all spectra, and absolute integral values were recorded and used for kinetic analysis. For resonances with small integrals, the baseline correction routine above resulted in negative integration values in some cases; therefore, a parallel baseline correction was performed with different parameters (filter: 50, 28.57 Hz; smooth factor: 3×10^4) to account for these features. Absolute integration values (y) over time (t) were plotted for each integration range and fitted using one of the following equations:

For the $A \rightarrow B \rightarrow C$ model:

$$A(t) = C_A \exp(-k_1 t)$$

$$B(t) = C_B \frac{k_1}{k_2 - k_1} [\exp(-k_1 t) - \exp(-k_2 t)]$$

$$C(t) = C_C \left\{ 1 - \frac{1}{k_2 - k_1} [k_2 \exp(-k_1 t) - k_1 \exp(-k_2 t)] \right\}$$

For the $A \rightarrow B \rightarrow C \rightarrow D$ model where only $C(t)$ and $D(t)$ are different from the previous model:

$$C(t) = C_C \frac{k_1 k_2}{k_2 - k_1} \left\{ \frac{\exp(-k_1 t) - \exp(-k_3 t)}{k_3 - k_1} - \frac{\exp(-k_2 t) - \exp(-k_3 t)}{k_3 - k_2} \right\}$$

$$D(t) = C_D \left\{ 1 - \frac{k_2 (k_3 \exp(-k_1 t) - k_1 \exp(-k_3 t))}{(k_3 - k_1)(k_2 - k_1)} + \frac{k_1 (k_3 \exp(-k_2 t) - k_2 \exp(-k_3 t))}{(k_3 - k_2)(k_2 - k_1)} \right\}$$

where A , B , C , and D are integrals as a function of time for resonance corresponding to the starting, intermediate, and product kinetic models for two- or three-step irreversible reactions; C_A , C_B , C_C , and C_D are arbitrary constants; and k_1 , k_2 , and k_3 are the rate constants for each reaction step.

UV–Visible Absorption Kinetic Experiments: Reaction of 4 with CO_2 . A Cary 50 spectrophotometer, equipped with Unisoku single-cell cryostat accessory to maintain the temperature within ± 0.1 °C, was used for all kinetics experiments. All measurements were performed in Schlenk-adapted cuvettes with a 1 cm optical path length. Baselines of all spectra were corrected by subtracting the spectrum of neat toluene at the same temperature. The typical procedure for sample preparation at variable temperatures is described below.

A stock solution of 2 or 4 and a magnetic stir bar were transferred to a solid addition flask, which was connected to a Schlenk cuvette in the glovebox. After five freeze–pump–thaw cycles, the solution was transferred to the cuvette, and the cuvette was placed in the Unisoku cryostat. UV–visible spectra were recorded until no further change was observed. CO_2 gas was introduced to the evacuated headspace immediately prior to starting the kinetic measurement, and the solution was agitated for 1 min to saturate the solution with CO_2 under atmospheric pressure. The concentration of saturated CO_2 was calculated or referred from the previous literature.^{42,43}

UV–visible spectra were recorded from 400–1000 nm with a 600 nm/min scan rate at a logarithmic time interval. The first point was discarded as the temperature, and the concentration of CO_2 had not been equilibrated. Kinetic traces for each reaction were generated by plotting absorbance (y) versus reaction time (t) at the peak wavelengths, which were analyzed using Origin v.8.5. Absorptions at 10 distinct wavelengths in the range of 405–495 nm with a 10 nm interval were chosen, and the curves were fitted to the first-order kinetic equations for two- or three-step irreversible reactions with shared parameters of rate constants:

For the two-step $A \rightarrow B \rightarrow C$ model:⁴⁴

$$\text{Abs}_{total}(t) = \text{Abs}_A(t) + \text{Abs}_B(t) + \text{Abs}_C(t)$$

$$= (\epsilon_A \exp(-k_1 t) + \epsilon_B \frac{k_1}{k_2 - k_1} [\exp(-k_1 t) - \exp(-k_2 t)] + \epsilon_C \left\{ 1 - \frac{1}{k_2 - k_1} [k_2 \exp(-k_1 t) - k_1 \exp(-k_2 t)] \right\}) \times [A]_0$$

where $[A]_0$, ϵ_A , ϵ_B , and ϵ_C are the initial concentration of the starting material and absorption constants of each A , B , and C species at a specified wavelength, and k_1 and k_2 are the pseudo-first-order rate constants.

This global analysis approach wherein the rate constants $k_{1,obs}$, $k_{2,obs}$, and $k_{3,obs}$ are shared over the wavelength range is critical because the rate constants tend to diverge to fit the absorption curves with convex and concave regions found in different reaction time courses at different wavelengths.

Electronic Structure Calculations. All electronic structure calculations were performed using ORCA v 4.1. Geometry optimizations and transition state searches were performed using

the BP86 level of theory using a broken-symmetry wave function, with the def2-tzvp basis set on all atoms, and Becke-Johnson damping function to account for dispersive forces (Grimme's D3). Geometry scans to identify starting structures for transition states and intermediates were performed by scanning the H–C bond for the insertion reaction and the Fe–O bond for the final rearrangement of the formate ligand to the monoformate product prior to transition state optimizations and intermediate geometry optimizations. Stationary points and transition states on the potential energy were verified by the absence of imaginary frequencies (stationary points) or the presence of one imaginary mode (transition state). Reported free energies were determined in a similar manner but used the PBE0 hybrid density functional as opposed to the BP86 density functional. Semiclassical room temperature ($T = 298.15$ K) H/D kinetic isotope effects (KIEs) were estimated by employing an Eyring model:

$$k_{\text{H}}/k_{\text{D}} = \exp[(\Delta G_{\text{D}}^{\ddagger} - \Delta G_{\text{H}}^{\ddagger})/RT]$$

To account for tunneling effects, a Wigner correction⁴⁵ to the semiclassical KIEs was applied by multiplying the Eyring KIEs with an H/D tunneling ratio correction ($Q_{\text{H}}/Q_{\text{D}}$), where

$$Q_i = 1 + u_i^2/24$$

and:

$$u_i = h\nu_i/k_{\text{B}}T$$

where h is the Planck constant, k_{B} is the Boltzmann constant, and ν_i is the transition state imaginary frequency.

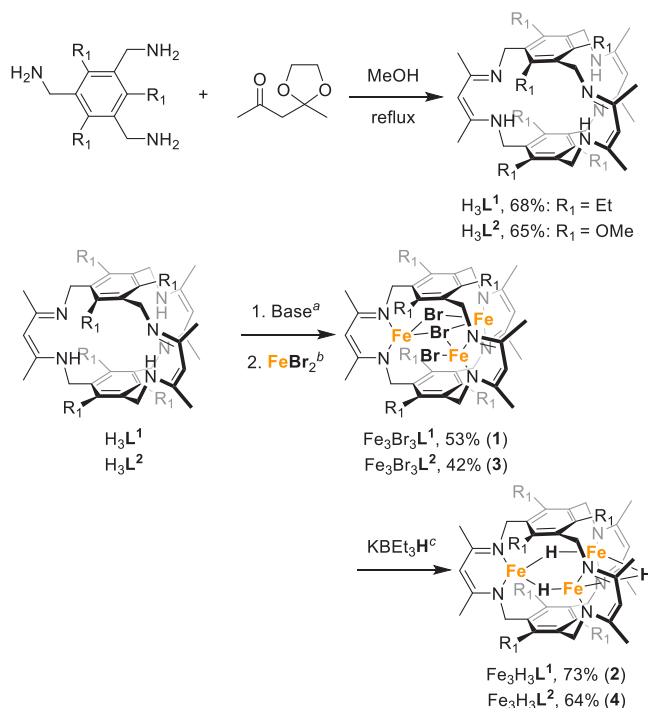
RESULTS AND DISCUSSION

Steric and Secondary Coordination Sphere Ligand Effect for CO₂ Insertion into Bridging Hydrides

Previously, we reported the significant through-space coupling between bridging the hydride and –CH₂– of ethyl substituents in the Zn isomer of Fe₃H₃L¹ (2).⁴⁶ To tune the sterics and electrostatics of the pocket surrounding the hydride donor, ligand H₃L² and the corresponding triiron complexes, Fe₃Br₃L² (3) and Fe₃H₃L² (4), were prepared in which the ethyl substituents on the two arene caps are replaced with methoxy groups (Scheme 2).^{29,38} Substituting the ethyl groups for a smaller methyl group or a proton yield ligands with poor solubility; thus, we opted for an ethyl for methoxy substitution to probe the role of sterics on reactivity. The crystallographic structure of 3 shows successful metalation of the three β-diketiminate arms (Figure S16).³⁸ The structures of the [Fe₃Br₃N₆] cores in 1 and 3 are isostructural with a minimal RMSD value of 0.34 between the two compounds (Figure 1a). The position of the terminal bromide contributes the most to this calculated RMSD as it resides much closer to the adjacent iron center in 3 than in 1 (4.329 vs 5.224 Å, Figure 1a). Complexes 1 and 3 support our assertion that variations to the ligand architecture can be readily accomplished without sacrificing access to isostructural complexes.

The Mössbauer spectrum for a solid sample of 3 recorded under a zero-applied field is well-simulated with a pair of quadrupole doublets centered at 0.90 and 0.93 mm·s⁻¹ with ΔE_{Q} values of 2.47 and 1.72 mm·s⁻¹, respectively, which are comparable to those obtained for 1 (0.95–1.02 mm·s⁻¹; Figure 1b). The 2:1 ratio for the integrals of these Mössbauer absorptions suggests that Fe1 and Fe3 are equivalent with Fe2 as unique (Figure 1a). The difference between the isomer shifts for 1 and 3 are attributed to greater fluxional behavior of the bromide donors and flexibility afforded by the OMe-for-Et substitution in 3 as compared to 1, which allows for interconversion between C_s and C_{2v} structures (the latter being a ladder-like configuration with the bromides as two μ-

Scheme 2. Ligand and Complex Synthesis



^aBenzyl potassium for H₃L¹, LDA for H₃L², r.t. in THF, 10 min. ^b80 °C for 1, 50 °C for 2 in C₇H₈, 20 h. ^cr.t. in C₇H₈, 10 min.

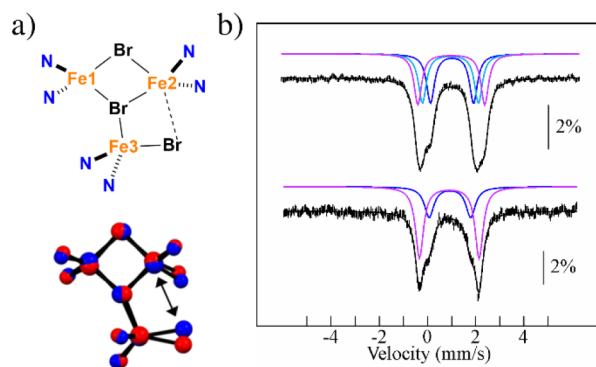


Figure 1. (a) Structure comparison of the [Fe₃Br₃N₆] core of 1 (red) and 3 (blue). Two-headed arrow highlights the narrowed distance between iron and terminal bromide of 3. (b) Mössbauer spectrum of Fe₃Br₃L¹ (1, top) and Fe₃Br₃L² (3, bottom). The black noisy lines represent the experimental data. The colored lines are simulated quadrupole doublets, as described in the text (see Table S1 for simulation parameters), whereas the black solid line is a composite spectrum obtained by combining individual doublets.

and one μ₃). Zero-applied field spectra recorded on a solid sample of 4 were best fit with a single quadrupole doublet centered at 0.78 mm·s⁻¹ with a quadrupole splitting of 2.27 mm·s⁻¹, consistent with the anticipated D_{3h} molecular symmetry (Figure S15, Table S1).²⁹ These parameters are in excellent agreement with those obtained for 2 (*viz.* δ = 0.79 mm·s⁻¹, $\Delta E_{\text{Q}} = 2.34$ mm·s⁻¹) and are consistent with tetrahedral-ligated high-spin iron(II) centers.^{29,47–49} Gratifyingly, the similar parameters of 4 and 2 support that there is minimal, if any, interaction between the Fe centers and the methoxy O atoms in 4. We conclude then that our ligand design is an effective secondary coordination sphere

perturbation, allowing targeted evaluation of pocket electrostatic or steric effects on hydride reactivity.

An initial survey of the reactivity of **4** toward CO₂ evidenced the faster reaction rate as compared to **2** with the same substrate under a dynamic atmosphere of CO₂ (Scheme 3 and

Scheme 3. Reaction Product of Trihydride Complexes (**2** or **4**) with CO₂

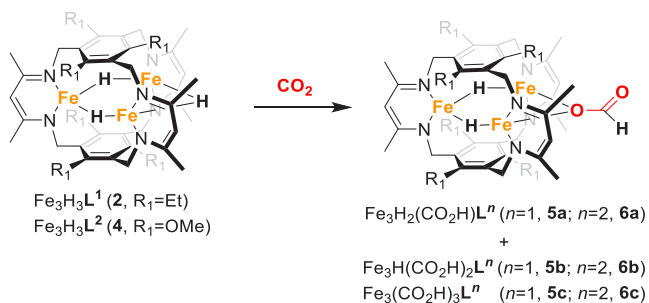


Figure S11).²⁹ To investigate the reaction kinetics and the intermediates formed during the reaction with CO₂, we exposed a degassed solution of **4** in benzene-*d*₆ to CO₂ at 293–308 K, agitated the solution to minimize the saturation time, and monitored the reaction by *in situ* ¹H NMR spectroscopy using hexamethylbenzene as an internal standard. All well-resolved peaks between –200 to 250 ppm in the

recorded spectra over the time course were integrated and plotted vs time. Grouping resonances by their time constants, we infer the presence of three kinetically related species after the addition of CO₂ (Figure 2). The four resonances associated with the *D*_{3h} symmetric **4** decreased exponentially with the concomitant increase in intensity of 11 new signals of the first intermediate (**6a**). The concentration of **6a** maximized at ~30 min, then decreased over the subsequent 15 h with the concomitant appearance of 10 new resonances of the second intermediate (**6b**). The intensities of **6b** maximized at ~15 h and decreased over the subsequent 7 days to afford seven new signals corresponding to a third species. From the independent reaction under a dynamic CO₂ atmosphere, the resonances for this final product are those for the *C*_{3v} symmetric triformate complex **6c**. These data imply that the reaction follows a four-component three sequential step reaction model (i.e., $A \rightarrow B \rightarrow C \rightarrow D$), with the two intermediates **6a** and **6b** corresponding to the mono- and diformato-triiron complexes, respectively.

To simplify our kinetic analysis, we flooded the reaction with CO₂ and fit the integrals of the resonances for each of the four observed species as a function of time using a pseudo-first order $A \rightarrow B \rightarrow C \rightarrow D$ model (Figure 2 and Table 1). From the spectra recorded at 25 °C, the integrals for resonances corresponding to **4** decrease exponentially and are well fit with the proposed model to afford $k_{1,\text{obs}} = 2.1(2) \times 10^{-3} \text{ s}^{-1}$, which is 20 times faster than that of **2** (*viz.* $1.1(1) \times 10^{-4} \text{ s}^{-1}$, Table

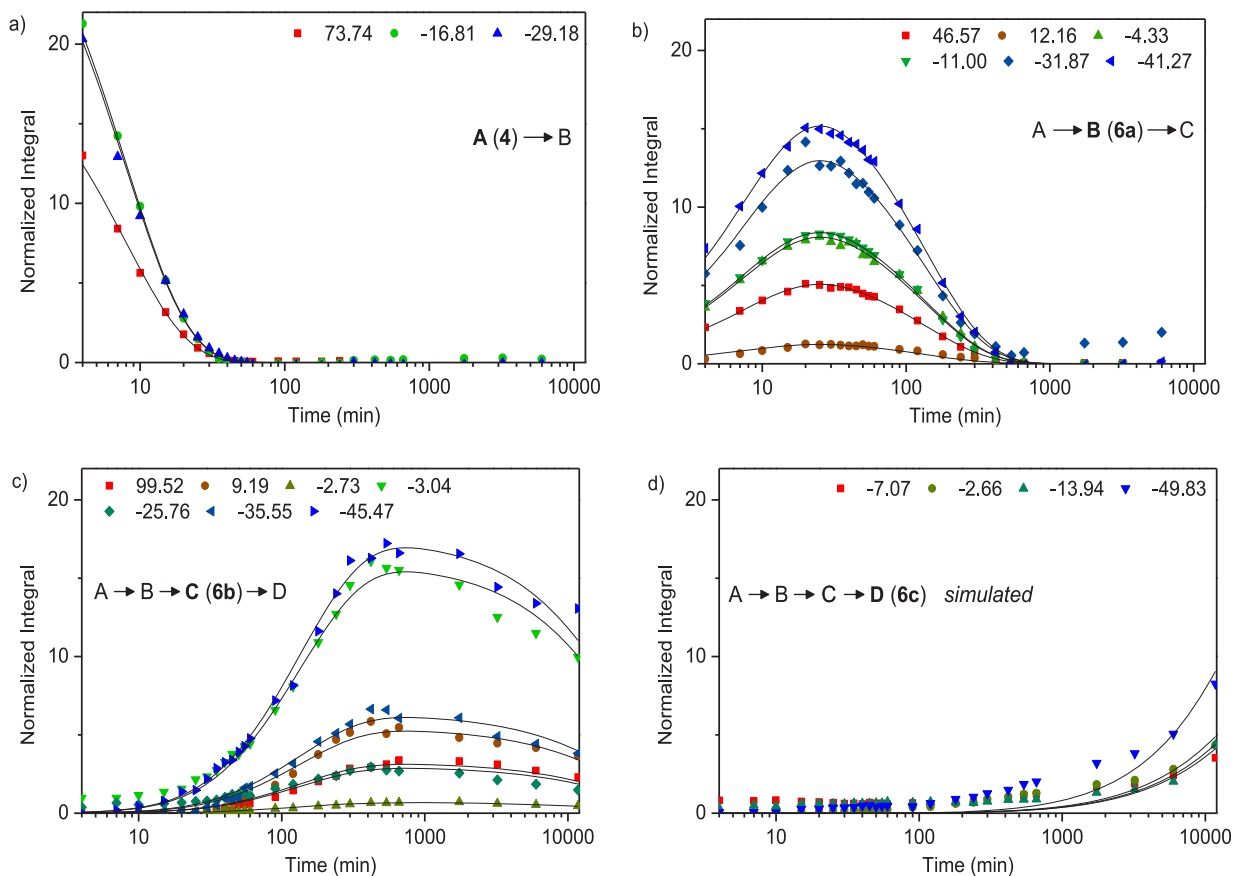


Figure 2. Changes of ¹H NMR integration values grouped by species **4** (a), **6a** (b), **6b** (c), and **6c** (d) for reaction of **4** with CO₂ (95 mM) in benzene-*d*₆ at 25 °C. Resonances are specified in the legend for which the integrations were fit using an $A \rightarrow B \rightarrow C \rightarrow D$ as described in the experimental section. Fitted rate constants from **4**, **6a**, and **6b** were used to simulate the data for **6c**. Each set of points represents the integration for the corresponding chemical shift as described in the legend. Peaks with minor contributions are omitted for clarity.

Table 1. Rate Constants Determined for Conversion of 4 to 6a by CO₂ in Benzene

method	[CO ₂] ^a (mM)	T (K)	fitting target	k _{1,obs} (× 10 ⁻³ s ⁻¹)	k ₁ (× 10 ⁻² M ⁻¹ ·s ⁻¹)
NMR	105	298	4	2.1(2)	2.0(2)
	105	298	6a	2.0(2)	1.9(2)
	105	298	6b	1.2(2)	1.1(2)
UV- vis	110	293	405–495 nm	1.6(1)	1.4(1)
	105	298		2.16(7)	2.05(7)
	100	303		2.82(7)	2.82(7)
	96	308		4.0(1)	4.2(1)

^aCalculated. See the [Experimental Section](#) for detail.

S4). From the kinetic model employed, we can also extract experimental values for $k_{1,obs}$ from kinetic profiles of **6a** and **6b**; the determined values of $2.0(2) \times 10^{-3} \text{ s}^{-1}$ and $1.2(2) \times 10^{-3} \text{ s}^{-1}$ for **6a** and **6b**, respectively, are comparable to that determined from the decay of **4**. The small $k_{1,obs}$ value of **6b** is attributed to underestimation of the integrals for resonances of **6b** at early reaction times (<2 h), as these peaks are broad and poorly resolved (Figure S17). An identical value of $k_{2,obs}$ of $1.2(1) \times 10^{-4} \text{ s}^{-1}$ was determined from the decay and formation of **6a** and **6b**. The formation of **6c** is too slow for reliable determination or modeling of the rate constants. Changing one hydride in **6a** to a formate in **6b** results in a 10-fold decrease in the rate of CO₂ insertion, implying that the electronic environment of the iron center plays an important role in the reaction.

We also employed variable temperature UV/visible spectrophotometry of reaction mixtures to measure the rate constants for these sequential reactions independently (and validate our NMR methodology) as well as to determine the activation parameters for the reaction of **4** with CO₂. The spectra were modeled using the sequential four-component kinetic model as above and globally fitted the absorption vs time data. Unlike the NMR kinetic analysis, deleterious reactions which introduce minor quantities of as-yet-identified side products were observed for all steps, but common rate constants for the 4-to-**6c** pathway were consistent between methods. This difference likely arises from trace impurities in the gas stream coupled to the differences in the scale and static vs dynamic atmospheres used for the NMR and UV/visible

experiments. Nonetheless, the first reaction rate constant ($k_{1,obs}$) determined from the NMR and UV/visible data is in excellent agreement; however, the second rate constant ($k_{2,obs}$) appears overestimated as we cannot separate this rate constant from contributions of those for an unproductive decomposition side reaction. Consequently, our variable-temperature data allow determination of ΔH^\ddagger , ΔS^\ddagger , and ΔG_{298K}^\ddagger values for the first CO₂ insertion event only; these values are 12.1(5) kcal·mol⁻¹, -26(2) e.u., and 19.7(7) kcal·mol⁻¹, respectively. Using the previously reported thermodynamic activation parameters for CO₂ insertion into **2**,⁵⁰ we surmise that the difference in the free energies of activation for CO₂ insertion for **2** and **4** ($\Delta\Delta G_{298K}^\ddagger = 1.7 \text{ kcal/mol}$) arises almost exclusively from the larger enthalpy of activation with $\Delta\Delta H^\ddagger = 2.6 \text{ kcal/mol}$ for **2** vs **4**. These data then suggest comparable order within both transition states, as one might expect given that **1** and **3** are isostructural, and that the steric or electrostatic changes resulting from the OMe for Et substitution reflect a decrease in the energetic cost to assemble the transition state.

The methoxy for ethyl substitution can influence the sterics and the electrostatics of the pocket surrounding the bridging hydride. To dissect which effect likely dominates here, we employed SambVca to estimate the buried volume around the bridging hydride in **2** and **4**.⁵¹ In the absence of a crystal structure for **4** but armed with spectroscopic data equivalent to **2**, we modeled **4** as replacing the CH₂ units in the ethyl substituents of **2** to O atoms. The resultant buried volumes calculated for these structures were 82.8% for **2** and 80.1% for **4** (Figure 3).^{52,53} We note that the 20-fold increase in $k_{1,obs}$ correlates with a ~3% reduction of the buried volume. A series of nickel pincer complexes are reported to have a 500- to 647-fold rate enhancement for inner-sphere CO₂ insertion—including the interaction between a metal center and CO₂ in the transition state—upon reducing the buried volume around the terminal hydride by 6–7%,⁴³ suggesting that the modest acceleration observed for **4** compared to **2** is consistent with primarily a steric effect. Decreasing the sterics of the pocket also serves to increase access to the metal centers, and we cannot discriminate between the possible contributions of steric accessibility to the hydride vs metal ion; that is, rate enhancements as a function of sterics may be similar for both inner and outer sphere pathways.

Solvent and Lewis Acid Effect for CO₂ Insertion. Choice of the reaction solvent or addition of cations can

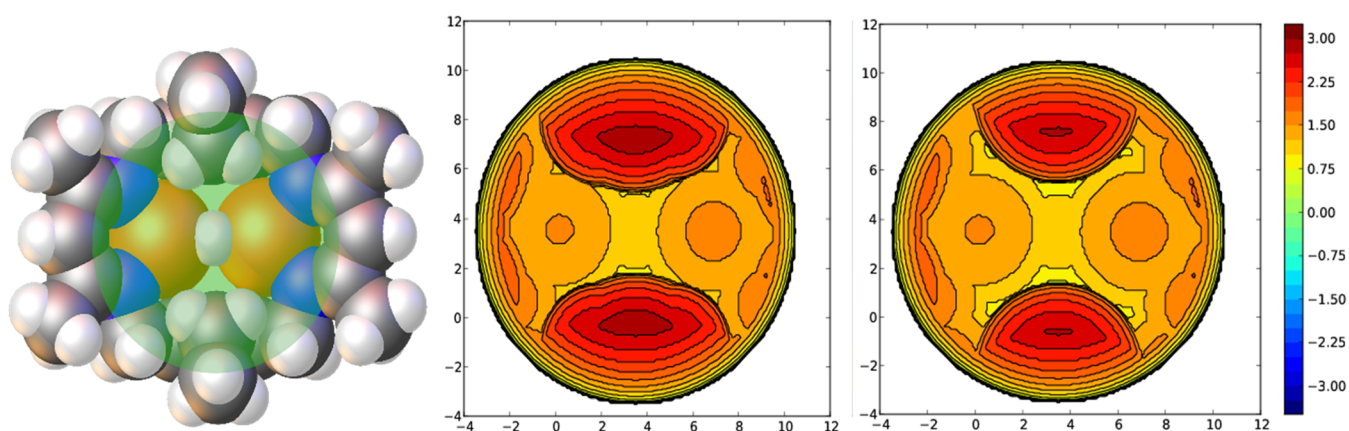


Figure 3. Affected area for the topographic steric maps around the bridging hydride of **2** (left, green circle) and the maps of **2** (middle, %V_{Bur} = 82.8%) and **4** (right, %V_{Bur} = 80.1%). C, N, H, and Fe are represented as gray, blue, white, and orange spheres with atomic radii, respectively.

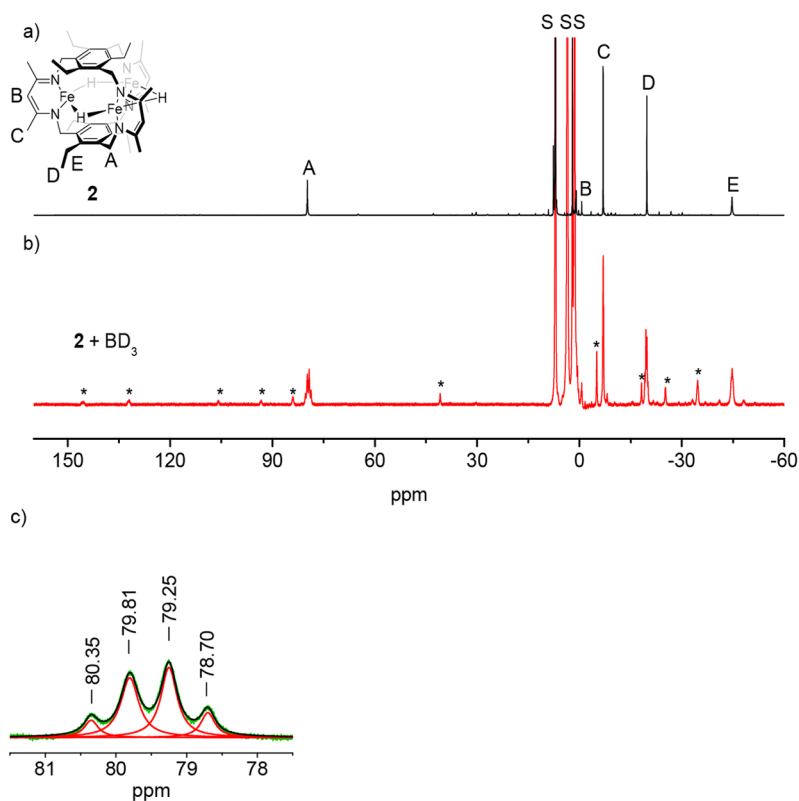


Figure 4. (a) ^1H NMR spectrum of **2** in toluene- d_8 . Peaks are marked as follows: $-\text{CH}_2-$ of aminomethyl A, $-\text{CH}-$ of beta-ketiminate B, CH_3- of β -ketiminate C, CH_3- of ethyl D, $-\text{CH}_2-$ of ethyl E, and solvent and solvent impurities S. (b) ^1H NMR spectrum from mixing equimolar amounts of **2** and deuterated borane THF adduct ($\text{BD}_3\cdot\text{THF}$) in toluene- d_8 for 20 h. Peaks from the minor species are denoted as *. All four isotopologues (H_3 , H_2D , HD_2 , and D_3) are visible as two groups of four nearby peaks at A (c) in a statistical 1:3:3:1 ratio, which are located in spatial vicinity to the bridging hydrides/deuterides. Relative intensities were determined through the deconvolution of the peak with Lorentzian functions (green, ^1H NMR spectrum; red, fitted Lorentzian functions for each component; black, sum of all component functions). Only the parts of the spectra from δ 160 to -60 ppm are shown for clarity.

enhance the rate of the CO_2 insertion into terminal hydride complexes when a charge is developed for the reaction intermediate.^{8,43,54,55} Dielectric constants (ϵ) of the solvents have been employed to correlate with the rate enhancement by the stabilization of the polar intermediate;⁵⁶ however, ANs ^{43,54,57,58} and solvatochromic constants ($E_T(30)$)⁵⁵ have also been considered for transition metal mediated transformations. We examined diethyl ether, benzene, 1,4-dioxane, tetrahydrofuran, and acetonitrile as solvents for the reaction of **2** with CO_2 (Figure S31 and Table S5). We observe the changes to the rate constant $k_{1,\text{obs}}$ as a function of reaction solvent, but there is no discernible correlation between $k_{1,\text{obs}}$ and any of the parameters ϵ , AN, or $E_T(30)$. Likewise, the addition of alkali cations has a negligible effect on the rate (Table S6). We also compared the effect of anions and ionic strength and, again, observed rate constants that are within error of reactions lacking such additives. We conclude that the reaction must either be proceeding with minimal charge accumulation on the O atom of the CO_2 substrate molecule—inconsistent with an outer-sphere pathway—or there is limited steric access of solvents and exogenous cations to the reaction center.

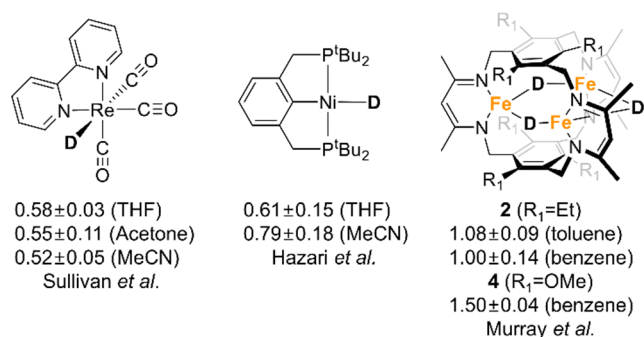
Estimating Thermodynamic Hydricity of **2.** To isolate the hydride insertion event from the thermodynamic compensation afforded by formate coordination, we estimated the hydricity of the Fe–H–Fe units by the reaction of **2** with a series of boranes. We envisioned this hydride abstraction

reaction to proceed by an outer sphere hydride transfer pathway. We selected the following boranes as these compounds cover a broad range of hydricities: BEt_3 (24), BPh_3 (36), BD_3 (50), and tris(pentafluorophenyl)borane or BCF (65). The values in parentheses are the calculated hydricities of conjugate borohydrides in $\text{kcal}\cdot\text{mol}^{-1}$ determined by DFT-level simulations.⁵⁹ Whereas complex **2** is unreactive toward BEt_3 (as expected given the synthetic route to **2**) and BPh_3 , complete consumption of **2** is observed by ^1H NMR spectroscopy upon reaction with BCF (Figure S12). We then examined the reaction with BD_3 insofar as the hydricity of borane is intermediate between BPh_3 and BCF. Here, we elected to use BD_3 rather than BH_3 to evaluate the reversibility of hydride abstraction.^{35,60} The reaction of **2** with BD_3 in toluene resulted in broad distribution of isotopologues of **2** based on the number of satellite peaks, which appear for each resonance corresponding to **2** (Figure 4). For example, the peaks at 80 ppm and -20 ppm are each well resolved into four peaks with the ratio of the integrals being 1:3:3:1. This ratio suggests a statistical mixture of available isotopically labeled complexes (*viz.* $[\text{Fe}_3\text{H}_3]^{3+}$, $[\text{Fe}_3\text{H}_2\text{D}]^{3+}$, $[\text{Fe}_3\text{D}_2\text{H}]^{3+}$, and $[\text{Fe}_3\text{D}_3]^{3+}$) results from the reversible hydride–deuteride exchange. In addition, new resonances are also observed in the region of 150 to -50 ppm, which could arise from complex products with reduced symmetry, as one might anticipate for a cationic triiron dihydride compound or a borohydride adduct. Given the equilibrium mixture observed and the near

equivalent distribution of the various isotopologues, we estimate the hydricity of **2** as comparable to that of borane and consistent with precedent.⁶¹ Given that $\Delta G_{\text{H}^-}(\text{HCOO}^-) = 44 \text{ kcal}\cdot\text{mol}^{-1}$ and the estimated hydricity for **2**, the reaction of **2** with CO_2 requires formate coordination to compensate for an otherwise endergonic CO_2 insertion in the Fe–H bonds in **2**. Previously, the bond dissociation free energy for an Fe–OC(O)H bond in a mononuclear iron complex was estimated at -8 kcal/mol , and a similar bond strength would be sufficient to favor the observed CO_2 to formate conversion here.⁶²

Kinetic Isotope Effect for CO_2 Insertion. We measured the kinetic isotope effect (KIE) for the first CO_2 insertion step to investigate the contribution of the hydride transfer in transition state. Deuteride complexes, **2-D₃** and **4-D₃**, were prepared by the reaction of LiBEt_3D with the bromide complexes, **1** and **3**. Previously, we communicated the KIE of 1.08(9) for reaction **2** with CO_2 in toluene (Scheme 4).⁵⁰

Scheme 4. Hydride Complexes with Reported KIE Values for CO_2 Insertion



We redetermined the KIE for the reaction in benzene to nullify any potential effect from solvent and to isolate the effect of the OMe-for-Et substitution on KIE. A value of 1.0(1) was obtained for **2/2-D₃** within the limits of error on our previous measurement. One anticipates that an outer-sphere mechanism is likely to have a substantial kinetic isotope effect arising from formation and cleavage of C–H and M–H bonds, respectively, in the transition state. Indeed, inverse KIE values were reported for CO_2 insertion into terminal hydride complexes of rhenium or nickel, and the lack of a KIE for **2** and a small normal KIE for **4** imply that an outer sphere mechanism is unlikely (Scheme 4).^{43,56}

The KIE near to unity is intriguing since it suggests two plausible scenarios: (1) hydride transfer from iron to carbon minimally contributes to the transition state⁶³ or (2) the late transition state has a similar zero-point energy gap as the starting material and is reflected in the bond dissociation free energies of the C–H being formed and the Fe–H bond(s) being broken. The comparable hydricities of **2** and CO_2 are consistent with the second scenario, although one might anticipate a larger primary KIE. Consistent with appreciable hydride transfer in the transition state, we observe an increase of the KIE to 1.50(4) upon reducing the steric crowding of the pocket as in **4/4-D₃**. These KIE results and the observed first order dependence on $[\text{CO}_2]$ can be rationalized based on the relative rates for an initial association of the CO_2 with the iron center as compared to the hydride transfer step, although any changes in hydride coordination during the reaction will complicate this analysis. Specifically, reduced steric pressure around the Fe center enhances the rate of CO_2 binding relative to hydride transfer, resulting in a greater observed contribution of the Fe–H bond cleavage and C–H bond forming to the overall activation barrier. Having exhausted the kinetic

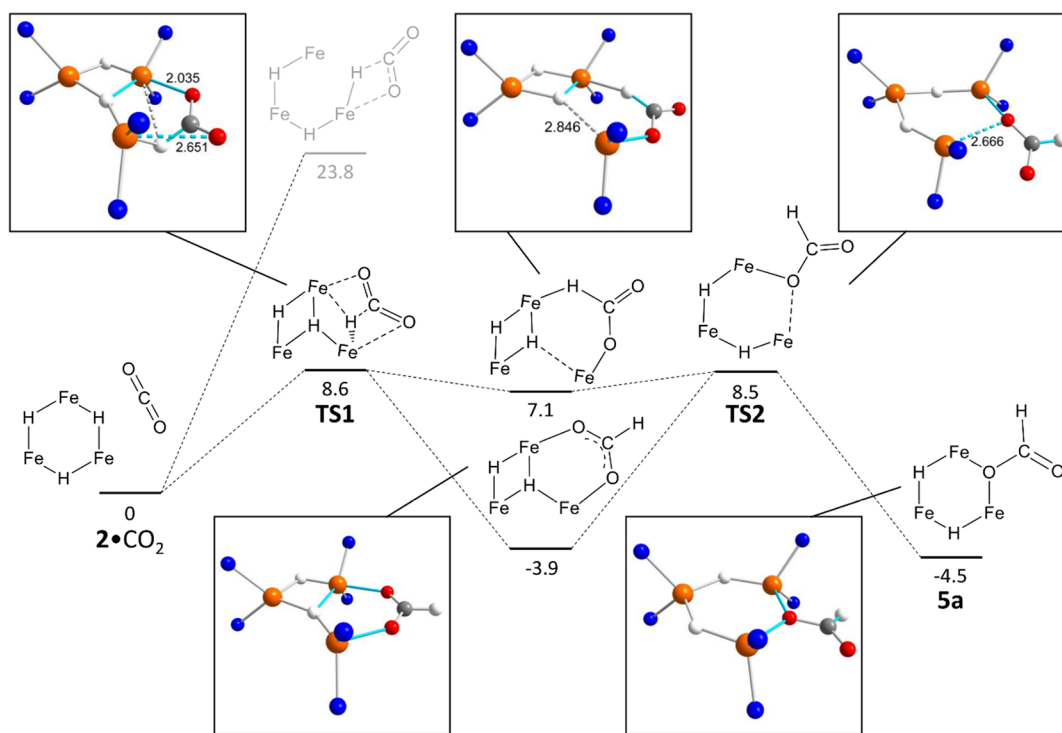
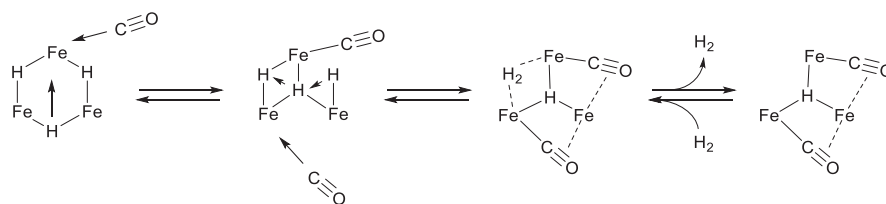


Figure 5. Hydride insertion mechanism for the conversion of **2** + CO_2 to **5a** showing the rearrangement of the Fe_3H_3 core. Free energies are given in $\text{kcal}\cdot\text{mol}^{-1}$. Inset figures display ball-and-stick configuration of metal clusters. C, N, O, H, and Fe are represented as gray, blue, red, white, and orange spheres. Bonds formed during the reaction are represented as sky-blue sticks.

Scheme 5. Proposed Associative Pathway for H₂/CO Exchange

methodologies at our disposal, we sought to complement and elucidate the mechanistic details using density functional methods.

Computationally Derived Reaction Pathway. To improve our understanding of CO₂ insertion by these trihydride complexes, we computationally explored the hydride transfer reaction between **2** and CO₂ to yield **5a** to construct viable mechanisms for formate formation. Geometry optimizations of **2** and **5a** using a broken symmetry wave function (PBE0/def2-tzvp/D3) yielded structures that were consistent with the crystallographic data obtained for the two complexes. Both compounds were found to be weakly antiferromagnetically coupled with $J = -116.23$ (**2**) and -27.15 cm⁻¹ (**5a**). We therefore utilized a broken symmetry approximation for transition state searches and the optimization of intermediate structures.

Attempts to construct reaction pathways for hydride insertion into CO₂ by **2** yielded two viable mechanisms involving the direct insertion of a hydride into the CO₂ molecule (Figure 5). In both viable mechanisms, we find that CO₂ forms a weak van der Waals complex with **2**, **2**·CO₂, with the CO₂ molecule associating within a pocket formed by two of the ethyl arms of the aromatic rings. There is no bonding interaction between the two iron atoms and CO₂ from analysis of the Laplacian of the electron density of **2**·CO₂. Alternate mechanisms, such as a CO₂ adduct formed with the central C atom of a BDI arm, were not apparent from our calculations. CO₂ insertion with minimal rearrangement of the Fe₃H₃ core affords a first transition state that is substantially higher in energy than that for a mechanism involving a coordination mode change for one hydride donor (23.8 kcal mol⁻¹ vs 8.6 kcal mol⁻¹ relative to **2**·CO₂). There, a ~7 kcal mol⁻¹ difference between the experimentally derived activation free energy and the activation free-energy of the rate-determining step in the low-energy pathway is a reasonable deviation from the experiment considering the approximations used in the computational model.⁶⁴ H/D KIEs for the first step of the reaction were estimated by replacing the hydride H with D in the calculated structures and then employing an Eyring model to which the tunneling correction of Wigner was applied.⁴⁵ The higher energy pathway yielded a calculated H/D KIE = 5.0, while the lower energy pathway yielded a calculated H/D KIE = 1.8. Given both its activation energy and calculated KIEs, we chose to focus on the lower-energy pathway for further analysis; however, we note that neither pathway can be ruled out based on the available data and the approximations/assumptions made in both the computational model and KIE calculations.

As the CO₂ molecule approaches a bridging hydride in the lower energy pathway, one of the oxygen atoms of CO₂ associates with an iron atom with a shift in coordination mode of a hydride from a μ to a μ_3 mode. After traversing **TS1**, the reaction branches with two possible intermediates formed,

differing in energy by 11.0 kcal mol⁻¹. The higher energy intermediate ($\Delta G = 7.1$ kcal mol⁻¹ relative to **2**·CO₂) comprises a monodentate terminal formate, whereas the lower energy intermediate ($\Delta G = -3.9$ kcal mol⁻¹) results from a rotation of the formate with the formate bound in a μ -1 κ O,2 κ O' or μ -1,3 mode. These two intermediates evolve to virtually indistinguishable transition states ($\Delta G^\ddagger = 8.5$ kcal mol⁻¹), resulting in the formation of the product **5a** ($\Delta G = -4.5$ kcal mol⁻¹ relative to **2**·CO₂).

Although the higher energy reaction pathway was not explored in detail, both mechanisms involve association of an oxygen atom from CO₂ with one of the iron atoms in the Fe₃H₃ core. Furthermore, the calculated Fe–O interaction at **TS1** is consistent with the observed insensitivity of the reaction to exogenous Lewis acids insofar as an intramolecular one is present. We surmise that the sterics of the pocket which influence the Fe–O interactions in **TS1** and **TS2** lead to the differences between the KIE for reaction of **2** vs **4** with CO₂. The reduced steric bulk of the hydride pocket in **4** as compared to **2** results in a greater contribution of Fe–H cleavage and C–H bond formation to **TS1** as compared to the association of CO₂ with the cluster and reduces the barrier to reorientation of the formate to a bridging coordination mode as it progresses through **TS2**.

Implications for Reactivity of Polynuclear Iron Hydrides. From our computational studies, the Fe₃H₃ cluster readily distorts to a μ_3 mode with minimal energy input, implying that these weak field ligated metal hydrides are quite fluxional. We posit that the hydride coordination modes change in response to the local electronic environment of any one metal center within the cluster. Focusing on the structure of **TS1**, a comparison to our previous report of reaction of **2** highlights this idea. Two hydrides shift coordination modes upon interaction with the Lewis acidic C atom of the CO₂ substrate. In **TS1**, the lengthening of one Fe–H bond and formation of an Fe–O interaction occur together with the shift of a second hydride to the central μ_3 position. One can envision that the interaction with CO₂ serves to effectively trap the μ_3 -hydride, allowing for the downstream reaction. Such an interpretation would be consistent with the reaction of **2** with CO, wherein H₂ is reductively eliminated and the final product contains a μ_3 hydride (Scheme 5). One possibility is the capture of a transient short-lived (μ_3 -hydrido)-di(μ -hydrido)-triiron(II) species by either CO₂ or CO. Coordination to an Fe center is envisioned in the case of CO, whereas the interaction of the Lewis acidic C of CO₂ with one μ -hydride leads to Fe–H bond elongation and ultimate cleavage. Alternatively, the coordination modes change upon interaction with the substrate; that is, electronic changes at the Fe centers upon substrate binding effect the shift. In either model, the substrate must present a Lewis basic site to stabilize the μ_3 -hydride isomer. Indeed, the observed hydricity and the near concomitant need for a donor is consistent with the lack of

reactivity of **2** with other substrates (e.g., Me₃SiCCH, C₂H₂, and CH₃CN), despite evidence that ligand sterics in other complexes of this ligand (*viz.* intermediate formed from Cu₃(N₂)L¹ with O₂) do not preclude reaction with substantially larger substrates (e.g., dihydroanthracene).²⁹ Although we cannot rigorously exclude a rapid pre-equilibrium between two conformers of the Fe₃H₃ core (*viz.* all μ -H and a less symmetric structure), such a scenario would be challenging to reconcile with the results reported here and that in prior reactivity studies of **2**. Indeed, the absence of scrambling of the hydride ligands between **2** and its tri(deuteride) isotopologue suggests that similar fluxional coordination is not accessible in this system as compared to the related tri(μ -sulfide) compound.⁶⁵ In the case of CO₂, hydride transfer is the ultimate outcome to generate formate, whereas the π -acidity of the CO donor favors a reductive elimination pathway. Thus, the coordinative plasticity of the hydrides in this polyiron polyhydride leads to common structure types from which the reaction outcome can bifurcate. Such plasticity is likely a common theme with weak field ligated polyiron systems^{28,33,35,36} and underpins the reactivity of the various reduced states of FeMoco.⁴ Similar rearrangement of the hydrides at the E₄ state could access a hydride-decorated dinitrogen bound form of FeMoco to liberate H₂.⁷ In addition, the observed plasticity in this polyiron system is reminiscent of the facile migration of H adatoms on metal surfaces, such as those competent for dinitrogen fixation,⁶⁶ implying that such molecular systems are useful models for catalysis at metal surfaces.

CONCLUSION

In summary, we demonstrated that the marked effect of metal ion access toward hydride transfer in an iron hydride cluster and, notably, the role of minor changes in the sterics from ethyl in **2** to methoxy in **4** within the secondary coordination sphere of the metal centers on the specificity toward CO₂ over other substrates. Indeed, reaction of **4** with the [Fe₃H₃]³⁺ cluster, which shares the D_{3h}-symmetric structure with Fe₃H₃L¹ (**2**) as confirmed by ¹H NMR and Mößbauer spectra, presented a 20-fold enhanced rate for the reaction with CO₂.

In the reaction for the hydride transfer from **2** to CO₂, the critical role of CO₂ binding to an iron center is supported by marginal KIE and insensitivity of added salts. The donor-free hydricity of **2**, estimated as 50 kcal·mol⁻¹ by the hydride-deuteride exchange with BD₃, is larger than that of formate (44 kcal·mol⁻¹) and supports the key role of Fe–O bond formation on the overall reaction progress. This experimental result is confirmed by computational methods, in which the structure of **TS1** arises from formation of a μ_3 hydride with the coordination of O to Fe. These results point to similar effects in other hydride-bridged polynuclear metal species and offer a strategy for the designed control of reactivity in such species.

ASSOCIATED CONTENT

Supporting Information

The Supporting Information is available free of charge at <https://pubs.acs.org/doi/10.1021/acs.inorgchem.1c00244>.

FT-IR, ¹H NMR, ¹³C{¹H} NMR, and ESI-MS spectra of the products; kinetic analysis; and crystal structures (PDF)

Accession Codes

CCDC 2043492 contains the supplementary crystallographic data for this paper. These data can be obtained free of charge via www.ccdc.cam.ac.uk/data_request/cif, or by emailing data_request@ccdc.cam.ac.uk, or by contacting The Cambridge Crystallographic Data Centre, 12 Union Road, Cambridge CB2 1EZ, UK; fax: +44 1223 336033.

AUTHOR INFORMATION

Corresponding Authors

Leslie J. Murray – Center for Catalysis and Florida Center for Heterocyclic Chemistry, Department of Chemistry, University of Florida, Gainesville, Florida 32611, United States; orcid.org/0000-0002-1568-958X; Email: murray@chem.ufl.edu

Jason Shearer – Department of Chemistry, Trinity University, San Antonio, Texas 78212, United States; orcid.org/0000-0001-7469-7304; Email: jshearer@trinity.edu

Authors

Dae Ho Hong – Center for Catalysis and Florida Center for Heterocyclic Chemistry, Department of Chemistry, University of Florida, Gainesville, Florida 32611, United States

Ricardo B. Ferreira – Center for Catalysis and Florida Center for Heterocyclic Chemistry, Department of Chemistry, University of Florida, Gainesville, Florida 32611, United States

Vincent J. Catalano – Department of Chemistry, University of Nevada, Reno, Nevada 89557, United States; orcid.org/0000-0003-2151-2892

Ricardo García-Serres – Université Grenoble Alpes, CNRS, CEA, BIG, LCBM (UMR 5249), F-38054 Grenoble, France; orcid.org/0000-0001-5203-0568

Complete contact information is available at: <https://pubs.acs.org/10.1021/acs.inorgchem.1c00244>

Notes

The authors declare no competing financial interest.

ACKNOWLEDGMENTS

D. H. H., R. B. F., and L. J. M. acknowledge the National Institutes of Health (R01-GM123241). Mass spectrometry data were collected by the University of Florida Mass Spectrometry Research and Education Center on instrumentation purchased with an award from the National Institutes of Health (S10 OD021758-01A1). The content is solely the responsibility of the authors and does not necessarily represent the official views of the National Institutes of Health. J. S. acknowledges National Science Foundation (CHE-1854854). R. G. S. acknowledges Labex ARCANE (ANR-11-LABX-0003-01).

REFERENCES

- (1) Schilter, D.; Camara, J. M.; Huynh, M. T.; Hammes-Schiffer, S.; Rauchfuss, T. B. Hydrogenase Enzymes and Their Synthetic Models: The Role of Metal Hydrides. *Chem. Rev.* **2016**, *116* (15), 8693–8749.
- (2) Reijerse, E. J.; Pham, C. C.; Pelmentschikov, V.; Gilbert-Wilson, R.; Adamska-Venkatesh, A.; Siebel, J. F.; Gee, L. B.; Yoda, Y.; Tamazaku, K.; Lubitz, W.; Rauchfuss, T. B.; Cramer, S. P. Direct Observation of an Iron-Bound Terminal Hydride in [FeFe]-Hydrogenase by Nuclear Resonance Vibrational Spectroscopy. *J. Am. Chem. Soc.* **2017**, *139* (12), 4306–4309.
- (3) Appel, A. M.; Bercaw, J. E.; Bocarsly, A. B.; Dobbek, H.; DuBois, D. L.; Dupuis, M.; Ferry, J. G.; Fujita, E.; Hille, R.; Kenis, P. J. A.;

Kerfeld, C. A.; Morris, R. H.; Peden, C. H. F.; Portis, A. R.; Ragsdale, S. W.; Rauchfuss, T. B.; Reek, J. N. H.; Seefeldt, L. C.; Thauer, R. K.; Waldrop, G. L. Frontiers, Opportunities, and Challenges in Biochemical and Chemical Catalysis of CO₂ Fixation. *Chem. Rev.* **2013**, *113* (8), 6621–6658.

(4) Khadka, N.; Dean, D. R.; Smith, D.; Hoffman, B. M.; Raugei, S.; Seefeldt, L. C. CO₂ Reduction Catalyzed by Nitrogenase: Pathways to Formate, Carbon Monoxide, and Methane. *Inorg. Chem.* **2016**, *55* (17), 8321–8330.

(5) Nishibayashi, Y. Recent Progress in Transition-Metal-Catalyzed Reduction of Molecular Dinitrogen under Ambient Reaction Conditions. *Inorg. Chem.* **2015**, *54* (19), 9234–9247.

(6) Hoffman, B. M.; Lukoyanov, D.; Yang, Z.-Y.; Dean, D. R.; Seefeldt, L. C. Mechanism of Nitrogen Fixation by Nitrogenase: The Next Stage. *Chem. Rev.* **2014**, *114* (8), 4041–4062.

(7) Rohde, M.; Sippel, D.; Trncik, C.; Andrade, S. L. A.; Einsle, O. The Critical E4 State of Nitrogenase Catalysis. *Biochemistry* **2018**, *57* (38), 5497–5504.

(8) Bernskoetter, W. H.; Hazari, N. Reversible Hydrogenation of Carbon Dioxide to Formic Acid and Methanol: Lewis Acid Enhancement of Base Metal Catalysts. *Acc. Chem. Res.* **2017**, *50* (4), 1049–1058.

(9) Sordakis, K.; Tang, C.; Vogt, L. K.; Junge, H.; Dyson, P. J.; Beller, M.; Laurency, G. Homogeneous Catalysis for Sustainable Hydrogen Storage in Formic Acid and Alcohols. *Chem. Rev.* **2018**, *118* (2), 372–433.

(10) Boddien, A.; Mellmann, D.; Gärtner, F.; Jackstell, R.; Junge, H.; Dyson, P. J.; Laurency, G.; Ludwig, R.; Beller, M. Efficient Dehydrogenation of Formic Acid Using an Iron Catalyst. *Science* **2011**, *333* (6050), 1733–1736.

(11) Nielsen, M.; Alberico, E.; Baumann, W.; Drexler, H.-J.; Junge, H.; Gladiali, S.; Beller, M. Low-Temperature Aqueous-Phase Methanol Dehydrogenation to Hydrogen and Carbon Dioxide. *Nature* **2013**, *495* (7439), 85–89.

(12) Jia, H.-P.; Quadrelli, E. A. Mechanistic Aspects of Dinitrogen Cleavage and Hydrogenation to Produce Ammonia in Catalysis and Organometallic Chemistry: Relevance of Metal Hydride Bonds and Dihydrogen. *Chem. Soc. Rev.* **2014**, *43* (2), 547–564.

(13) Klankermayer, J.; Wesselbaum, S.; Beydoun, K.; Leitner, W. Selective Catalytic Synthesis Using the Combination of Carbon Dioxide and Hydrogen: Catalytic Chess at the Interface of Energy and Chemistry. *Angew. Chem., Int. Ed.* **2016**, *55* (26), 7296–7343.

(14) Qiao, J.; Liu, Y.; Hong, F.; Zhang, J. A Review of Catalysts for the Electroreduction of Carbon Dioxide to Produce Low-Carbon Fuels. *Chem. Soc. Rev.* **2014**, *43* (2), 631–675.

(15) Ceballos, B. M.; Yang, J. Y. Directing the Reactivity of Metal Hydrides for Selective CO₂ Reduction. *Proc. Natl. Acad. Sci. U. S. A.* **2018**, *115* (50), 12686–12691.

(16) Deutsch, C.; Krause, N.; Lipshutz, B. H. CuH-Catalyzed Reactions. *Chem. Rev.* **2008**, *108* (8), 2916–2927.

(17) Ye, Y.; Kim, S.-T.; Jeong, J.; Baik, M.-H.; Buchwald, S. L. CuH-Catalyzed Enantioselective Alkylation of Indole Derivatives with Ligand-Controlled Regiodivergence. *J. Am. Chem. Soc.* **2019**, *141* (9), 3901–3909.

(18) Lukoyanov, D. A.; Khadka, N.; Yang, Z.-Y.; Dean, D. R.; Seefeldt, L. C.; Hoffman, B. M. Hydride Conformers of the Nitrogenase FeMo-Cofactor Two-Electron Reduced State E₂(2H), Assigned Using Cryogenic Intra Electron Paramagnetic Resonance Cavity Photolysis. *Inorg. Chem.* **2018**, *57* (12), 6847–6852.

(19) Brecht, M.; van Gestel, M.; Buhrke, T.; Friedrich, B.; Lubitz, W. Direct Detection of a Hydrogen Ligand in the [NiFe] Center of the Regulatory H₂-Sensing Hydrogenase from *Ralstonia eutropha* in Its Reduced State by HYSCORE and ENDOR Spectroscopy. *J. Am. Chem. Soc.* **2003**, *125* (43), 13075–13083.

(20) Mebs, S.; Senger, M.; Duan, J.; Wittkamp, F.; Apfel, U.-P.; Happe, T.; Winkler, M.; Stripp, S. T.; Haumann, M. Bridging Hydride at Reduced H-Cluster Species in [FeFe]-Hydrogenases Revealed by Infrared Spectroscopy, Isotope Editing, and Quantum Chemistry. *J. Am. Chem. Soc.* **2017**, *139* (35), 12157–12160.

(21) Honkala, K.; Hellman, A.; Remediakis, I. N.; Logadottir, A.; Carlsson, A.; Dahl, S.; Christensen, C. H.; Nørskov, J. K. Ammonia Synthesis from First-Principles Calculations. *Science* **2005**, *307* (5709), 555–558.

(22) Ertl, G. Reactions at Surfaces: From Atoms to Complexity (Nobel Lecture). *Angew. Chem., Int. Ed.* **2008**, *47* (19), 3524–3535.

(23) Mager-Maury, C.; Bonnard, G.; Chizallet, C.; Sautet, P.; Raybaud, P. H₂-Induced Reconstruction of Supported Pt Clusters: Metal-Support Interaction versus Surface Hydride. *ChemCatChem* **2011**, *3* (1), 200–207.

(24) Churchill, M. R.; Bezman, S. A.; Osborn, J. A.; Wormald, J. Synthesis and Molecular Geometry of Hexameric Triphenylphosphinocopper(I) Hydride and the Crystal Structure of H₆Cu₆(PPh₃)₆·HCONMe₂ [Hexameric Triphenylphosphino Copper(I) Hydride Dimethylformamide]. *Inorg. Chem.* **1972**, *11* (8), 1818–1825.

(25) Dhayal, R. S.; van Zyl, W. E.; Liu, C. W. Polyhydrido Copper Clusters: Synthetic Advances, Structural Diversity, and Nanocluster-to-Nanoparticle Conversion. *Acc. Chem. Res.* **2016**, *49* (1), 86–95.

(26) Andres, H.; Bominaar, E. L.; Smith, J. M.; Eckert, N. A.; Holland, P. L.; Münck, E. Planar Three-Coordinate High-Spin Fe^{II} Complexes with Large Orbital Angular Momentum: Mössbauer, Electron Paramagnetic Resonance, and Electronic Structure Studies. *J. Am. Chem. Soc.* **2002**, *124* (12), 3012–3025.

(27) DeRossa, D. E.; Mercado, B. Q.; Lukat-Rodgers, G.; Rodgers, K. R.; Holland, P. L. Enhancement of C-H Oxidizing Ability in Co-O₂ Complexes through an Isolated Heterobimetallic Oxo Intermediate. *Angew. Chem., Int. Ed.* **2017**, *56* (12), 3211–3215.

(28) Yu, Y.; Sadique, A. R.; Smith, J. M.; Dugan, T. R.; Cowley, R. E.; Brennessel, W. W.; Flaschenriem, C. J.; Bill, E.; Cundari, T. R.; Holland, P. L. The Reactivity Patterns of Low-Coordinate Iron-Hydride Complexes. *J. Am. Chem. Soc.* **2008**, *130* (20), 6624–6638.

(29) Lee, Y.; Anderton, K. J.; Sloane, F. T.; Ermer, D. M.; Abboud, K. A.; Garcia-Serres, R.; Murray, L. J. Reactivity of Hydride Bridges in High-Spin [3M-3(μ-H)] Clusters (M = Fe^{II}, Co^{II}). *J. Am. Chem. Soc.* **2015**, *137* (33), 10610–10617.

(30) Gehring, H.; Metzinger, R.; Braun, B.; Herwig, C.; Harder, S.; Ray, K.; Limberg, C. An Iron(II) Hydride Complex of a Ligand with Two Adjacent β-Diketiminato Binding Sites and Its Reactivity. *Dalton Trans.* **2016**, *45* (7), 2989–2996.

(31) Hein, N. M.; Pick, F. S.; Fryzuk, M. D. Synthesis and Reactivity of a Low-Coordinate Iron(II) Hydride Complex: Applications in Catalytic Hydrodefluorination. *Inorg. Chem.* **2017**, *56* (23), 14513–14523.

(32) Thompson, C. V.; Arman, H. D.; Tonzetich, Z. J. A Pyrrole-Based Pincer Ligand Permits Access to Three Oxidation States of Iron in Organometallic Complexes. *Organometallics* **2017**, *36* (9), 1795–1802.

(33) Ott, J. C.; Blasius, C. K.; Wadepohl, H.; Gade, L. H. Synthesis, Characterization, and Reactivity of a High-Spin Iron(II) Hydride Complex Supported by a PNP Pincer Ligand and Its Application as a Homogenous Catalyst for the Hydrogenation of Alkenes. *Inorg. Chem.* **2018**, *57* (6), 3183–3191.

(34) Anderton, K. J.; Knight, B. J.; Rheingold, A. L.; Abboud, K. A.; Garcia-Serres, R.; Murray, L. J. Reactivity of Hydride Bridges in a High-Spin [Fe₃(μ-H)₃]³⁺ Cluster: Reversible H₂/CO Exchange and Fe-H/B-F Bond Metathesis. *Chem. Sci.* **2017**, *8* (5), 4123–4129.

(35) Dugan, T. R.; Bill, E.; MacLeod, K. C.; Brennessel, W. W.; Holland, P. L. Synthesis, Spectroscopy, and Hydrogen/Deuterium Exchange in High-Spin Iron(II) Hydride Complexes. *Inorg. Chem.* **2014**, *53* (5), 2370–2380.

(36) Yu, Y.; Brennessel, W. W.; Holland, P. L. Borane B-C Bond Cleavage by a Low-Coordinate Iron Hydride Complex and N-N Bond Cleavage by the Hydridoborate Product. *Organometallics* **2007**, *26* (13), 3217–3226.

(37) Hong, D. H.; Knight, B. J.; Catalano, V. J.; Murray, L. J. Isolation of Chloride- and Hydride-Bridged Tri-Iron and -Zinc Clusters in a Tris(β-Oxo-δ-Diimine) Cyclophane Ligand. *Dalton Trans.* **2019**, *48*, 9570–9575.

- (38) Guillet, G. L.; Sloane, F. T.; Ermert, D. M.; Calkins, M. W.; Peparah, M. K.; Knowles, E. S.; Cizmar, E.; Abboud, K. A.; Meisel, M. W.; Murray, L. J. Preorganized Assembly of Three Iron(II) or Manganese(II) β -Diketiminato Complexes Using a Cyclophane Ligand. *Chem. Commun.* **2013**, 49 (59), 6635–6637.
- (39) Li, H.; Homan, E. A.; Lampkins, A. J.; Ghiviriga, I.; Castellano, R. K. Synthesis and Self-Assembly of Functionalized Donor- σ -Acceptor Molecules. *Org. Lett.* **2005**, 7 (3), 443–446.
- (40) Ruppel, S.; Schulte to Brinke, C.; Hahn, F. E. Synthesis and Coordination Chemistry of a Tris(Benzene-*o*-Dithiolato)- Functionalized Ligand as a Siderophore Analog. *Z. Naturforsch., B: J. Chem. Sci.* **2013**, 68 (5–6), 551–556.
- (41) Wallace, K. J.; Hanes, R.; Anslyn, E.; Morey, J.; Kilway, K. V.; Siegel, J. Preparation of 1,3,5-Tris(Aminomethyl)-2,4,6-Triethylbenzene from Two Versatile 1,3,5-Tri(Halosubstituted) 2,4,6-Triethylbenzene Derivatives. *Synthesis* **2005**, 2005 (12), 2080–2083.
- (42) Fogg, P. G. T. *Carbon Dioxide in Non-Aqueous Solvents At Pressures Less Than 200 KPA*; Elsevier, 1992, DOI: 10.1016/C2009-0-00247-5.
- (43) Heimann, J. E.; Bernskoetter, W. H.; Hazari, N.; Mayer, J. M. Acceleration of CO₂ Insertion into Metal Hydrides: Ligand, Lewis Acid, and Solvent Effects on Reaction Kinetics. *Chem. Sci.* **2018**, 9 (32), 6629–6638.
- (44) Espenson, J. *Chemical Kinetics and Reaction Mechanisms*, 2 ed.; McGraw-Hill Education: New York, 2002.
- (45) Lars, M.; William, H. S., Jr In *Reaction Rates of Isotopic Molecules*; Robert E. Krieger Publishing Company: Malabar, FL, 1987.
- (46) Ermert, D. M.; Ghiviriga, I.; Catalano, V. J.; Shearer, J.; Murray, L. J. An Air- and Water-Tolerant Zinc Hydride Cluster That Reacts Selectively With CO₂. *Angew. Chem., Int. Ed.* **2015**, 54 (24), 7047–7050.
- (47) Beinert, H.; Holm, R. H.; Münck, E. Iron-Sulfur Clusters: Nature's Modular, Multipurpose Structures. *Science* **1997**, 277 (5326), 653–659.
- (48) Dugan, T. R.; Holland, P. L. New Routes to Low-Coordinate Iron Hydride Complexes: The Binuclear Oxidative Addition of H₂. *J. Organomet. Chem.* **2009**, 694 (17), 2825–2830.
- (49) Albers, A.; Demeshko, S.; Pröpper, K.; Dechert, S.; Bill, E.; Meyer, F. A Super-Reduced Diferrous [2Fe-2S] Cluster. *J. Am. Chem. Soc.* **2013**, 135 (5), 1704–1707.
- (50) Hong, D. H.; Murray, L. J. Carbon Dioxide Insertion into Bridging Iron Hydrides: Kinetic and Mechanistic Studies. *Eur. J. Inorg. Chem.* **2019**, 2019 (15), 2146–2153.
- (51) Poater, A.; Cosenza, B.; Correa, A.; Giudice, S.; Ragone, F.; Scarano, V.; Cavallo, L. SambVca: A Web Application for the Calculation of the Buried Volume of N-Heterocyclic Carbene Ligands. *Eur. J. Inorg. Chem.* **2009**, 2009 (13), 1759–1766.
- (52) Poater, A.; Ragone, F.; Giudice, S.; Costabile, C.; Dorta, R.; Nolan, S. P.; Cavallo, L. Thermodynamics of N-Heterocyclic Carbene Dimerization: The Balance of Sterics and Electronics. *Organometallics* **2008**, 27 (12), 2679–2681.
- (53) Poater, A.; Ragone, F.; Mariz, R.; Dorta, R.; Cavallo, L. Comparing the Enantioselective Power of Steric and Electrostatic Effects in Transition-Metal-Catalyzed Asymmetric Synthesis. *Chem. - Eur. J.* **2010**, 16 (48), 14348–14353.
- (54) Creutz, C.; Chou, M. H. Rapid Transfer of Hydride Ion from a Ruthenium Complex to Cl Species in Water. *J. Am. Chem. Soc.* **2007**, 129 (33), 10108–10109.
- (55) Heimann, J. E.; Bernskoetter, W. H.; Hazari, N. Understanding the Individual and Combined Effects of Solvent and Lewis Acid on CO₂ Insertion into a Metal Hydride. *J. Am. Chem. Soc.* **2019**, 14110520.
- (56) Sullivan, B. P.; Meyer, T. J. Kinetics and Mechanism of Carbon Dioxide Insertion into a Metal-Hydride Bond. A Large Solvent Effect and an Inverse Kinetic Isotope Effect. *Organometallics* **1986**, 5 (7), 1500–1502.
- (57) Konno, H.; Kobayashi, A.; Sakamoto, K.; Fagalde, F.; Katz, N. E.; Saitoh, H.; Ishitani, O. Synthesis and Properties of [Ru(Tpy)(4,4'-X₂bpy)H]⁺ (Tpy = 2,2':6',2''-Terpyridine, Bpy = 2,2'-Bipyridine, X = H and MeO), and Their Reactions with CO₂. *Inorg. Chim. Acta* **2000**, 299 (2), 155–163.
- (58) Kang, P.; Cheng, C.; Chen, Z.; Schauer, C. K.; Meyer, T. J.; Brookhart, M. Selective Electrocatalytic Reduction of CO₂ to Formate by Water-Stable Iridium Dihydride Pincer Complexes. *J. Am. Chem. Soc.* **2012**, 134 (12), 5500–5503.
- (59) Heiden, Z. M.; Lathem, A. P. Establishing the Hydride Donor Abilities of Main Group Hydrides. *Organometallics* **2015**, 34 (10), 1818–1827.
- (60) Heintz, R. A.; Theopold, K. H.; Neiss, T. G. Unusually Large Isotope Effects on NMR Chemical Shifts of Paramagnetic Organometallic Compounds. *Angew. Chem., Int. Ed. Engl.* **1994**, 33 (22), 2326–2328.
- (61) Mock, M. T.; Potter, R. G.; Camaioni, D. M.; Li, J.; Dougherty, W. G.; Kassel, W. S.; Twamley, B.; DuBois, D. L. Thermodynamic Studies and Hydride Transfer Reactions from a Rhodium Complex to BX₃ Compounds. *J. Am. Chem. Soc.* **2009**, 131 (40), 14454–14465.
- (62) Fong, H.; Peters, J. C. Hydricity of an Fe-H Species and Catalytic CO₂ Hydrogenation. *Inorg. Chem.* **2015**, 54 (11), 5124–5135.
- (63) Gómez-Gallego, M.; Sierra, M. A. Kinetic Isotope Effects in the Study of Organometallic Reaction Mechanisms. *Chem. Rev.* **2011**, 111 (8), 4857–4963.
- (64) Liu, Z.; Patel, C.; Harvey, J. N.; Sunoj, R. B. Mechanism and Reactivity in the Morita-Baylis-Hillman Reaction: The Challenge of Accurate Computations. *Phys. Chem. Chem. Phys.* **2017**, 19 (45), 30647–30657.
- (65) Buratto, W. R.; Ferreira, R. B.; Catalano, V. J.; García-Serres, R.; Murray, L. J. Cleavage of cluster iron-sulfide bonds in cyclophane-coordinated Fe_nS_m complexes. *Dalton Trans.* **2021**, 50, 816–821.
- (66) Qian, J.; An, Q.; Fortunelli, A.; Nielsen, R. J.; Goddard, W. A. Reaction Mechanism and Kinetics for Ammonia Synthesis on the Fe(111) Surface. *J. Am. Chem. Soc.* **2018**, 140 (20), 6288–6297.